SENSORS

Cuttlefish eye–inspired artificial vision for high-quality imaging under uneven illumination conditions

Minsung Kim[1,2,3]†, Sehui Chang[4]†, Minsu Kim[1,2]†, Ji-Eun Yeo[4], Min Seok Kim[4], Gil Ju Lee[5]*, Dae-Hyeong Kim[1,2,6]*, Young Min Song[4,7]*

With the rise of mobile robotics, including self-driving automobiles and drones, developing artificial vision for high-contrast and high-acuity imaging in vertically uneven illumination conditions has become an important goal. In such situations, balancing uneven illumination, improving image contrast for facile object detection, and achieving high visual acuity in the main visual fields are key requirements. Meanwhile, in nature, cuttlefish (genus *Sepia*) have evolved an eye optimized for vertically uneven illumination conditions, which consists of a W-shaped pupil, a single spherical lens, and a curved retina with a high-density photoreceptor arrangement and polarized light sensitivity. Here, inspired by the cuttlefish eye, we report an artificial vision system consisting of a W-shaped pupil, a single ball lens, a surface-integrated flexible polarizer, and a cylindrical silicon photodiode array with a locally densified pixel arrangement. The W-shaped pupil integrated on the ball lens balances vertically uneven illumination, and the cylindrical silicon photodiode array integrated with the flexible polarizer enables high-contrast and high-acuity imaging.

INTRODUCTION

Artificial vision can play a pivotal role in mobile robotics, including self-driving automobiles (*1*, *2*), to monitor surrounding environments and to detect approaching objects for collision avoidance, which can partially or completely substitute for human vision that is vulnerable in constantly changing light conditions. For such applications, high detectability of objects is important, which generally requires high-contrast and high-acuity imaging systems (*3*, *4*). Camera-based vision systems have been implemented to support image detection because of their low cost, small form factor, and single-shot image capture capability (*5*). However, the limited image contrast, especially in vertically uneven illumination conditions due to intense sunlight scattering in the upper visual fields and randomly polarized sunlight noise reflected from glazed surfaces of surroundings (*6*, *7*), substantially hinders high-quality imaging and consequently leads to low object detectability (fig. S1A) (*8*). Whereas an automobile driver can physically block the intense upper sunlight and mitigate polarized noise with a sun visor and sunglasses (fig. S1B), respectively, artificial vision systems for mobile robots and autonomous vehicles should exploit software-based approaches to resolving such unfavorable light conditions (*6*). However, the large amount of visual information that the system should process requires high computational power and energy consumption (*9*, *10*). Therefore, appropriate hardware solutions are demanded to deal with nonhomogeneous light conditions, minimize polarized light noise, and reduce the amount of data processing.

Meanwhile, vision systems in nature have inspired the development of artificial vision systems with unique features (*11*–*14*). For example, aquatic and amphibious animals have evolved to have eyes optimized for their habitats, and these have inspired various artificial vision systems. Inspired by the panoramic imaging capability of fish eyes, a miniaturized wide field-of-view (FOV) imaging system that consists of a monocentric lens and a hemispherical silicon nanorod photodiode array has been developed (*4*). Inspired by the retina structure of the elephant-nose fish (*Gnathonemus petersii*), which can enhance the intensity of collected light in a low-light condition, a photosensitivity enhancer that consists of microphotocollectors has been developed (*15*). Inspired by the hyperspectral and polarimetric imaging strategy of mantis shrimp (such as *Odontodactylus scyllarus*), an image sensor that consists of polarization-sensitive organic photodetectors and folded polymer retarders has been developed (*16*). Inspired by the flat corneal microlenses and stalk-eye structure of a fiddler crab (*Uca arcuata*) living in the intertidal region, an all-weather imaging system with a 360° FOV, which is composed of multilayered flat microlenses and a spherical silicon photodiode array, has been developed (*17*). Despite such efforts for the development of diverse bioinspired artificial vision systems (*18*, *19*), one that can balance the vertically uneven illumination while achieving high contrast and acuity in highly noisy conditions due to randomly polarized sunlight has not yet been developed.

In this context, cuttlefish (genus *Sepia*), which have evolved to have a high-acuity vision system optimized for vertically uneven illumination and detection of polarized light (Fig. 1, A and B, respectively), inspire high-performance artificial vision for mobile robotics. Cuttlefish have a unique eye structure that consists of a W-shaped pupil (Fig. 2Ai), a single spherical lens (Fig. 2Aii), and a curved retina (Fig. 2Aiii) with a high-density belt-like photoreceptor region (Fig. 2B) and polarization-sensitive photoreceptors (Fig. 2B, right inset) (*20*–*22*). More information about the eyes of cuttlefishes and other coleoid cephalopods is provided in table S1.

[1]School of Chemical and Biological Engineering, Institute of Chemical Processes, Seoul National University, Seoul 08826, Republic of Korea. [2]Center for Nanoparticle Research, Institute for Basic Science (IBS), Seoul 08826, Republic of Korea. [3]Querrey Simpson Institute for Bioelectronics, Northwestern University, Evanston, IL 60208, USA. [4]School of Electrical Engineering and Computer Science, Gwangju Institute of Science and Technology, Gwangju 61005, Republic of Korea. [5]Department of Electronics Engineering, Pusan National University, Busan 46241, Republic of Korea. [6]Department of Materials Science and Engineering, Seoul National University, Seoul 08826, Republic of Korea. [7]AI Graduate School, Gwangju Institute of Science and Technology, Gwangju 61005, Republic of Korea.
*Corresponding author. Email: gjlee0414@pusan.ac.kr (G.J.L.); dkim98@snu.ac.kr (D.-H.K.); ymsong@gist.ac.kr (Y.M.S.)
†These authors contributed equally to this work.

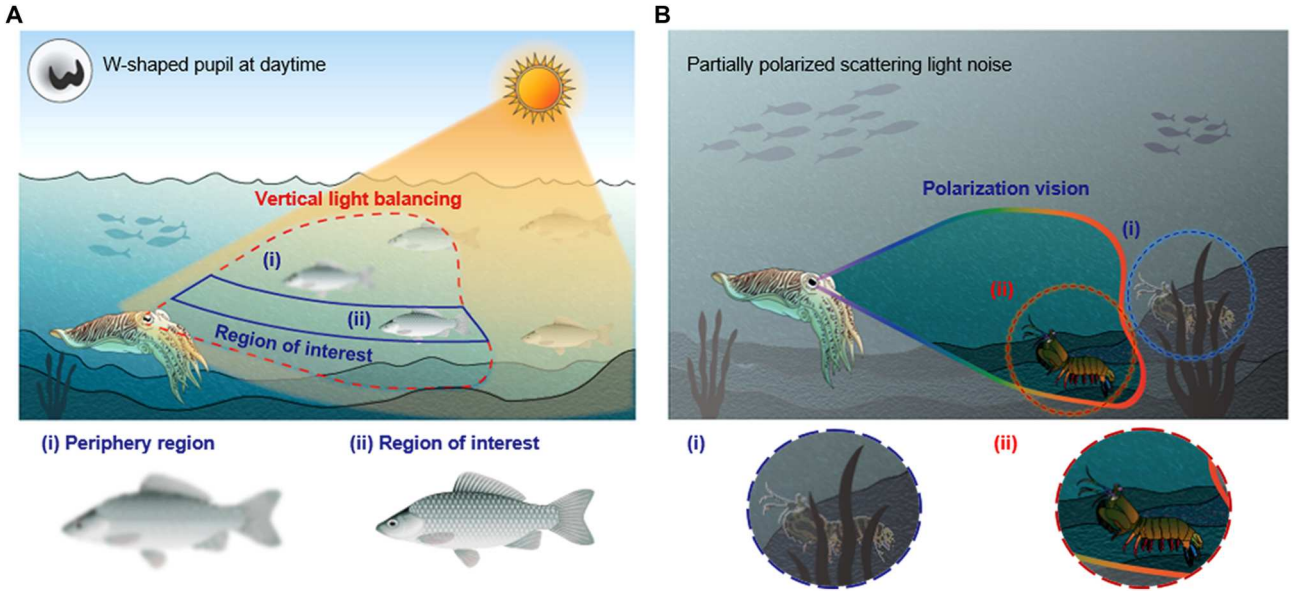

Fig. 1. Optical features of cuttlefish living in the underwater environment. (**A** and **B**) Schematic illustrations that depict the capability of cuttlefish vision to balance vertically uneven illumination in shallow-water habitats, to focus the ROI with high acuity, and to recognize polarized light for high contrast. Bottom insets of (A): (i) low-resolution fish image detected in the peripheral visual region and (ii) high-resolution fish image detected in the ROI. Bottom insets of (B): (i) mantis shrimp image detected by general vision and (ii) mantis shrimp image detected by polarization vision.

In daytime, the distinctive W-shaped pupil enables cuttlefish to have high-contrast vision by balancing out vertically uneven illumination (Fig. 1A, red dashed region). The high-density belt-like photoreceptor region (*23*) in the retina allows for high visual acuity in its region of interest (ROI) (Fig. 1A, ii versus i). This belt-like photoreceptor distribution is optimal for the detection of approaching objects near the horizon (*24*). In addition, the horizontally or vertically stacked microvilli of photoreceptors (*22*, *25*, *26*) allow for the cuttlefish to efficiently recognize camouflaged prey by extracting polarized light reflected from the target object and filtering out randomly polarized background noise (Fig. 1B, ii versus i), leading to enhanced visual contrast.

Inspired by such unique structural and functional features of the cuttlefish vision system, we herein report an artificial vision system that enables high-contrast and high-acuity imaging under vertically uneven illumination conditions for high-performance artificial vision for potential applications in mobile robotics. The W-shaped pupil in the artificial vision system compensates for the uneven vertical light distribution by reducing incident lights from the top of its vertical FOV. In addition, the cylindrical silicon photodiode array (c-Si-PDA), which includes the high-density belt-like pixel region, enables high-acuity imaging in the ROI. The flexible carbon nanotube (CNT)–polarizing film (FCPF) integrated on the surface of the c-Si-PDA maintains an average degree of polarization of ~78% in the visible wavelength range, which enables polarization-sensitive imaging. By integrating these optical and electronic components, we developed an artificial vision system that can balance the uneven light distribution while achieving high contrast and acuity (fig. S1C).

RESULTS

Artificial cuttlefish lens integrated with the W-shaped pupil

An artificial vision inspired by the cuttlefish eye was designed as an integrated system of a W-shaped pupil, two half-ball lenses with an aperture stop in the middle, and a c-Si-PDA. Detailed design parameters were determined according to the optical ray-tracing simulation results (Fig. 3A and table S2). A horizontally curved cylindrical image plane was adopted to emulate the high-contrast and high-acuity horizontal vision of the cuttlefish. Although the cylindrical plane results in relatively larger spot radii at the high vertical incident angles compared with those at the hemispherical plane, its horizontal spot radii are sufficiently smaller than those at the planar plane (fig. S2). Therefore, the cylindrical plane can realize high-quality horizontal vision. The ray-tracing result demonstrates that the incident light from the top side (i.e., magenta-colored rays in Fig. 3A) is mostly blocked by the W-shaped pupil, whereas the focal spots of other rays are formed well on the c-Si-PDA. Such spatially selective blocking by the W-shaped pupil balances vertically uneven light by shading strong incident light from the top side.

The artificial cuttlefish lens was constructed by assembling two N-BK7 half-ball lenses with an aperture stop in the middle (Fig. 3B). Commercial N-BK7 half-ball lenses with a diameter of 10 mm were used. Unlike the gradient refractive index ball lens of the cephalopod eye (*27*), a single/homogenous spherical glass ball lens suffers from various optical aberrations such as spherical aberration and coma. The aperture stop was inserted between two half-ball lenses, and its aperture diameter (i.e., 6 mm) was optimized not only to reduce inherent optical aberrations but also to sufficiently collect incident light within the target FOV [i.e., 120° horizontal (H) by 70° vertical (V)] (fig. S3). Cuttlefish can control the pupil size under ambient light conditions. The distinctive W-shape pupil, whose open area is ~20% of the entire area, is formed when the

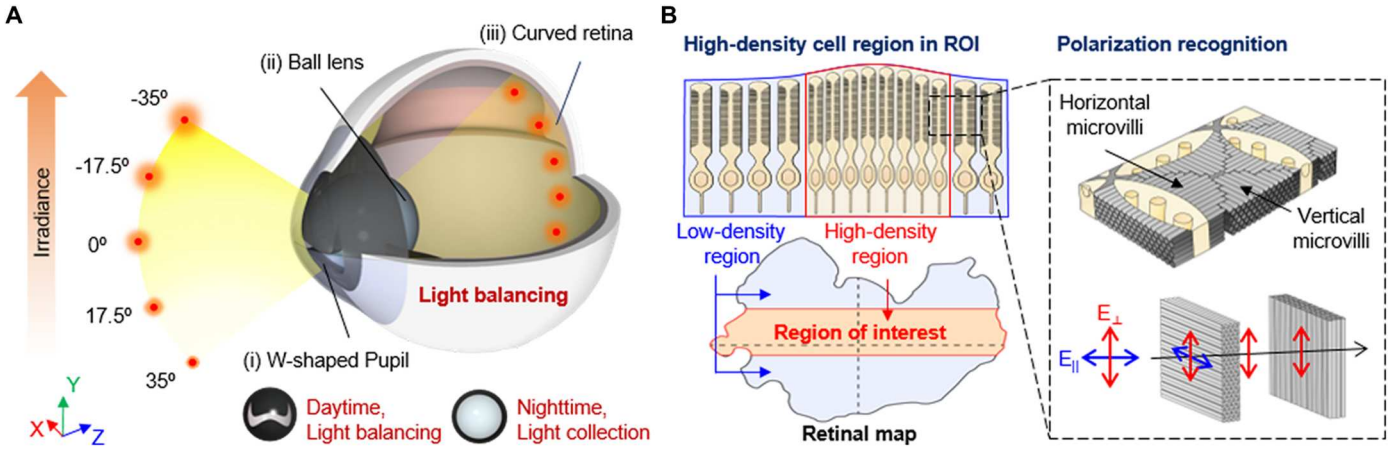

Fig. 2. Ocular structure of the cuttlefish, genus *Sepia*. (**A**) Schematic drawing of the cuttlefish eye that consists of a W-shaped pupil, a ball lens, and a curved retina. (**B**) Cross-sectional illustration of the uneven photoreceptor distribution in the cuttlefish retina (top). The high-density belt-like photoreceptor region is located slightly above the equator (bottom). Inset: The microvilli of adjacent photoreceptors are orthogonally arranged, which allows for detecting polarized light.

cuttlefish eye is exposed to bright light (*28*). This pupil condition was mimicked in the artificial pupil, and the open area of the artificial W-shaped pupil was designed to be ~20% of the entire lens area in the two-dimensional (2D) layouts. The interspace between two lenses and the aperture stop was filled with a transparent optical adhesive (NOA 61, Norland, USA). The front and back sides of the N-BK7 half-ball lenses are shown in Fig. 3C (left). The fabricated W-shaped pupil, circular pupil, and aperture stop are shown in Fig. 3C (right). A circular pupil, whose open area is the same as the open area of the W-shaped pupil, was also prepared for the control experiment (fig. S4). The assembled optical systems using the W-shaped pupil [W-shaped pupil–integrated imaging system (WPIS)] or the circular pupil [circular pupil–integrated imaging system (CPIS)] are shown in Fig. 3D.

The horizontally elongated open area in the W-shaped pupil provides a sharp image contrast in the horizontal contours, allowing a horizontally panoramic view that is suitable for the detection of horizontally approaching objects. According to the line spread function, the vertical resolution of the WPIS is higher than its horizontal resolution, whereas the CPIS shows similar resolutions in both directions (fig. S5A). Sharper horizontal lines can be seen in the imaging simulation of a grid pattern with the WPIS, which indicates its higher resolvability in the vertical direction than the horizontal direction (fig. S5B). More details about the imaging contrast of the W-shaped pupil are provided in figs. S6 and S7 and text S1.

In daytime, intense sunlight comes from the sea surface. In the shallow-water region (habitat of cuttlefish), the light intensity distribution changes substantially along the depth of water (fig. S8A) (*20*, *29*). The WPIS reduces the amount of incident light from the top side of its optical axis more than that from the bottom side, whereas the CPIS shows similar light intensity drops on both sides (Fig. 3E). For objects with vertically uneven brightness (Fig. 3F, inset, and fig. S8B), the irradiance distributions on the image plane were simulated for two imaging systems (Fig. 3F). In both the WPIS and the CPIS, the irradiance passing through the artificial pupils has a decreasing trend from the top visual field to the bottom for the object with the vertically uneven brightness. In the CPIS case, the irradiance is strong in the top area of the image plane (Fig. 3F, left), and its intensity decreases downward along the *y* direction as the irradiance of incident light decreases. In contrast, the irradiance in the WPIS case is relatively more balanced over the entire vertical visual field because the intense top light is reduced by the W-shaped pupil (Fig. 3F, right). Thus, the WPIS is more useful than the CPIS for imaging in environments with vertically uneven light distributions.

Polarization-recognizable c-Si-PDA

Inspired by the curved retina of the cuttlefish eye (Fig. 4A), the c-Si-PDA with a FCPF was designed and fabricated (Fig. 4B). First, an ultrathin image sensor array was fabricated on a flat substrate (fig. S9A), and then it was transfer-printed onto a cylindrically curved substrate (fig. S9B). Mechanical fractures could be prevented during the transfer process because of the ultrathin nature of the c-Si-PDA (~5.5 μm; fig. S10) (*4*). The detailed fabrication process is described in Materials and Methods and figs. S11 and S12. An individual pixel in the array consisted of a photodiode and a blocking diode, serially arranged with n-p-n configuration (Fig. 4C, inset). The current-voltage curves of a photodiode (without the polarization film) for various intensities of incident light and its dynamic range are presented in Fig. 4D and fig. S13, respectively.

The pixels in the c-Si-PDA can be grouped as a belt-like high-density region (Fig. 4E) and low-density regions around the high-density region (Fig. 4F). This pixel arrangement was mimicked from the photoreceptor distribution in the retina of *Sepia esculenta*. The cuttlefish retina has a belt-like region with densely packed visual cells slightly above the equator (Fig. 4A) (*23*). Similarly, the high–pixel density region was placed slightly above the centerline (fig. S14). Whereas the target ROI maintained a high pixel density, the visually less-important regions have a low pixel density, which can reduce the overall data processing load.

The natural cuttlefish eye can recognize the polarization state of incident light with the uniaxially aligned microvilli on top of the photoreceptor. In the artificial vision system, an FCPF acted as the artificial microvilli. Single-wall CNTs (SWCNTs), which have strong optical anisotropy (*30*), were used for the FCPF. The uniaxially aligned SWCNTs absorbed polarized light parallel to the aligned SWCNTs, whereas the optical absorption was suppressed for perpendicularly polarized light (fig. S15) (*31*). By aligning

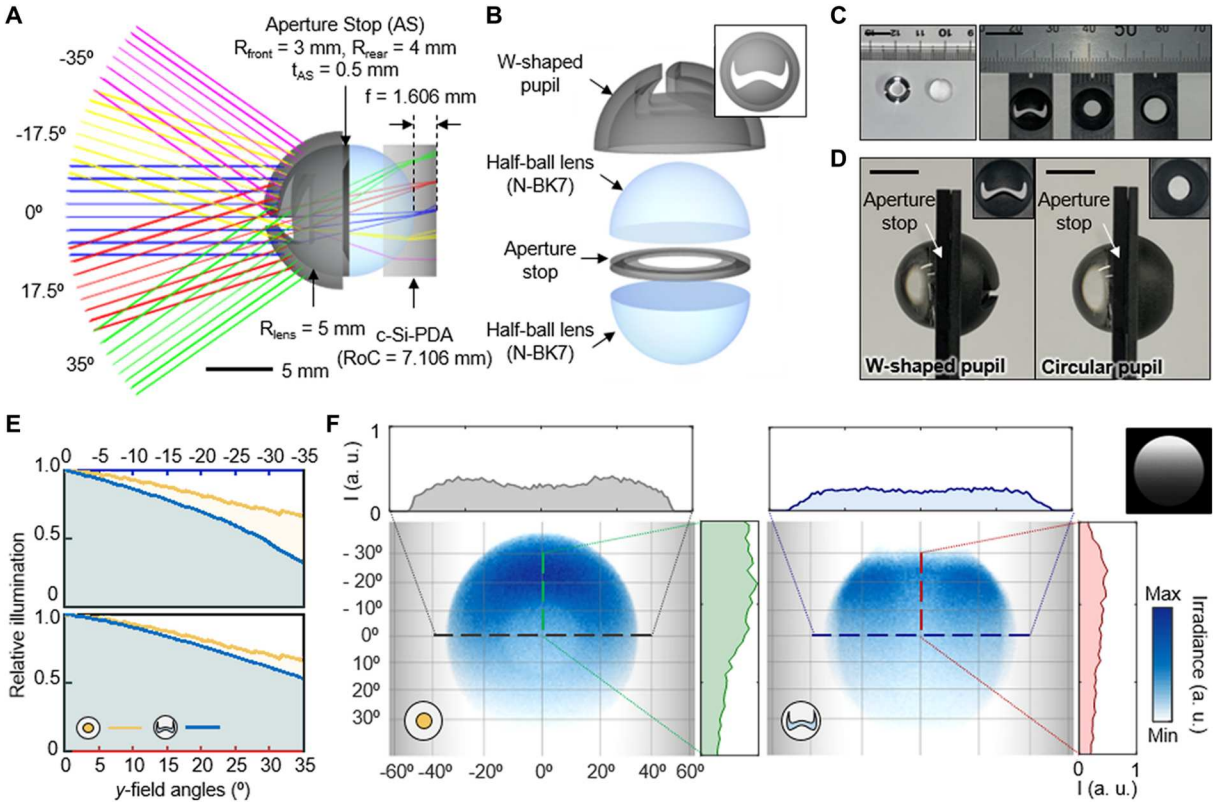

Fig. 3. Artificial cuttlefish lens with a W-shaped pupil. (**A**) Optical layout of the artificial cuttlefish lens designed by referring to ray-tracing simulation. (**B**) Exploded schematic illustrations of the artificial cuttlefish lens. (**C**) Photograph of the front and back sides of half-ball lenses (N-BK7) (left) and photograph of the W-shaped pupil, circular pupil, and aperture stop (right). Scale bars, 1 cm. (**D**) Photographs showing an integrated form of the artificial cuttlefish lens and the pupils (left, W-shaped pupil; right, circular pupil). Scale bars, 5 mm. (**E**) Relative illumination by the cuttlefish lens with the W-shaped pupil (blue) and with the circular pupil (yellow) for even incident illuminations. Top: Relative illumination graph along –*y*-field angles. Bottom: Relative illumination graph along +*y*-field angles. (**F**) Optical simulation for imaging a circular target object with vertically uneven illumination (right top inset). The graphs on the top and right sides show the irradiance intensity (*I*) profiles on the *x* and *y* axes.

SWCNTs inside the flexible polymer film poly(vinylidene fluoride-trifluoroethylene-chlorofluoroethylene) [P(VDF-TrFE-CFE)] via uniaxial stretching of the film, the polarization film can be made. For example, a homogenous mixture of SWCNTs, P(VDF-TrFE-CFE), and the solvent was drop-cast on a glass substrate, and then the nanocomposite film obtained after solvent evaporation was stretched for alignment of SWCNTs. More details of the fabrication are explained in Materials and Methods.

Transmittance spectra of the FCPF show strong optical anisotropy in the visible range (wavelength between 450 and 650 nm) (Fig. 4G). A high degree of polarization, up to ~78%, was achieved in this range (Fig. 4H). Note that stretching of the FCPF up to ~400% successfully aligns CNTs, whereas less-stretched FCPFs (e.g., ~300 or ~ 350%) show an insufficient degree of polarization (fig. S16). Optical camera images in Fig. 4I show the polarizing effect of the FCPF. An image of a cuttlefish was prepared by removing one polarization component in a liquid crystal display. A clear cuttlefish image could be seen when the SWCNT direction in the FCPF and the polarization direction of the image were perpendicular. However, when the FCPF was rotated by 90°, the cuttlefish image was barely seen. These results indicate that the FCPF successfully serves as a linear polarizer.

Because of its flexibility, the FCPF can be seamlessly integrated with the c-Si-PDA (Fig. 4B and cross-sectional view in fig. S17). To test the polarization-recognizable c-Si-PDA, the photocurrent of a c-Si-PDA with the FCPF was measured, whereas a commercial linear polarizer located in front of the light source was rotated (Fig. 4J). When the polarization direction of incident light was perpendicular to the SWCNT alignment direction of the FCPF, the measured photocurrent was ~58 nA (applied bias, ~3.2 V). However, when the directions of the incident polarized light and the SWCNTs in the FCPF were parallel, the measured photocurrent became negligible because the aligned CNTs blocked most of the incident polarized light.

Imaging demonstrations by the cuttlefish eye–inspired artificial vision system

All components of the cuttlefish eye–inspired artificial vision system (i.e., W-shaped pupil, ball lens, c-Si-PDA, and FCPF) were integrated in a custom-made housing. The schematic illustration and photographs (Fig. 5A) show an exploded view of the artificial vision system and images of the components, respectively. The c-Si-PDA integrated with the FCPF was interconnected to the external electronics through an anisotropic conductive film (ACF). The assembled device is shown in fig. S18, and its optical axis length was ~24.1 cm.

The artificial vision system has unique features inspired by the natural cuttlefish eye (Fig. 2), such as light-balancing capability

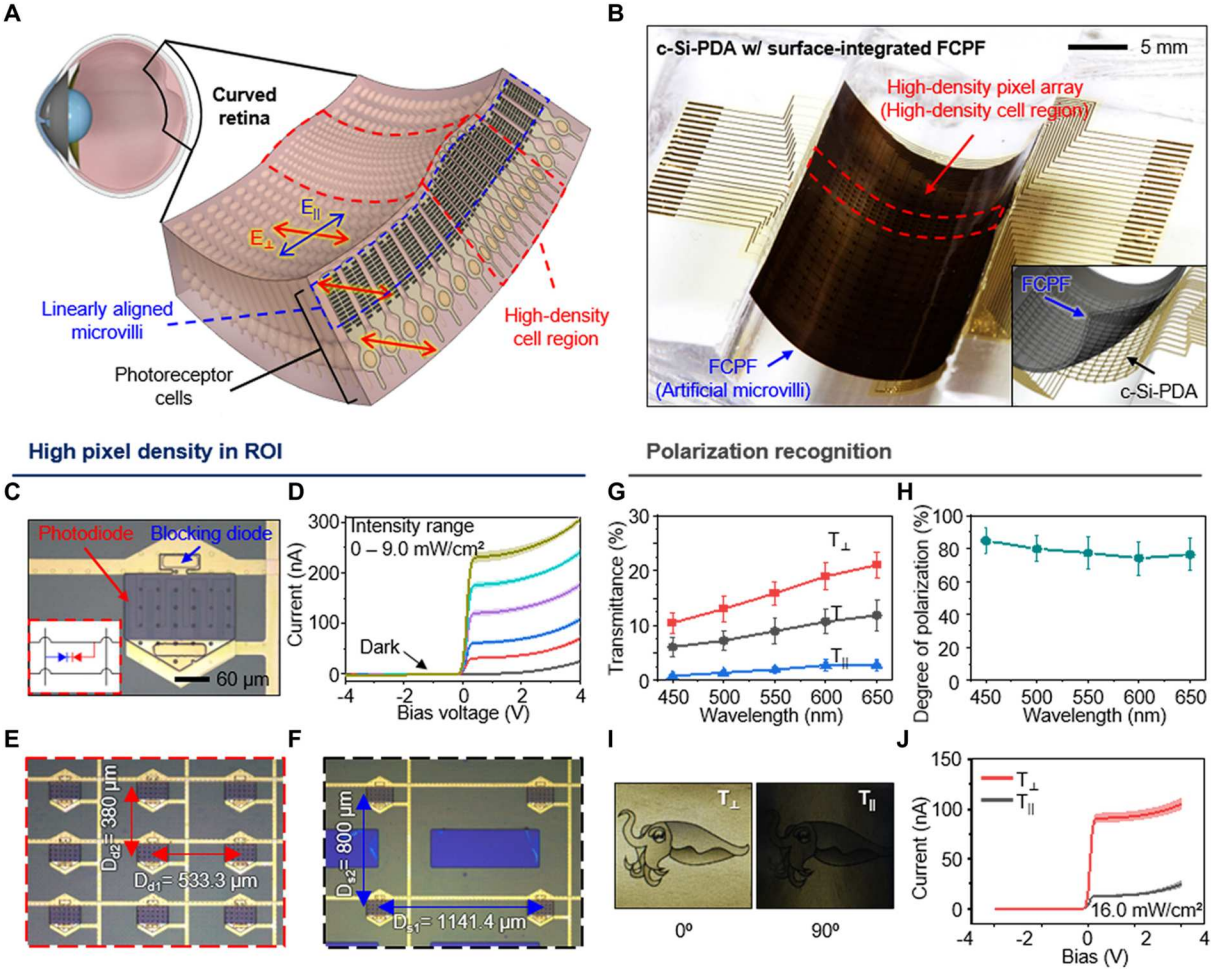

Fig. 4. c-Si-PDA with surface-integrated FCPF inspired by the cuttlefish retina. (**A**) Schematic illustration of the cross-sectional view of the cuttlefish retina. (**B**) Photograph of the fabricated Si photodiode array integrated with the FCPF on a cylindrical substrate (red dashed box, high-density region). Inset: Schematic illustration of the exploded view of the c-Si-PDA with an FCPF. (**C**) An optical microscopy image of an individual pixel that consists of a photodiode (red) and a blocking diode (blue). The inset shows a circuit diagram of an individual pixel. (**D**) Current (*I*)–voltage (*V*) curves of a Si photodiode with a blocking diode as the light intensity increases from 0 to 9.0 mW/cm^2. Shaded error bars represent SD of 10 individual pixels. (**E**) Optical microscopy image of the high–pixel density region. (**F**) Optical microscopy image of the low–pixel density region. (**G**) Transmittance spectra and (**H**) degree of polarization of the 400% stretched FCPF, which is selected as a representative sample in imaging demonstration. Error bars represent SD of five individual 400% stretched FCPFs. (**I**) Angular polarization characteristics of the FCPF. Optical camera images of the FCPF on a liquid crystal display (LCD). The linearly polarized light intensity of the cuttlefish image on the LCD is varied by rotating the FCPF, which acts as a linear polarizer. (**J**) *I*-*V* curves of the c-Si-PDA with surface-integrated FCPF under parallel-polarized ($T_{\parallel}$) and cross-polarized ($T_{\perp}$) lights with a light intensity of 16.0 mW/cm^2. Shaded error bars represent SD of 10 individual pixels.

under vertically uneven illumination conditions by the W-shaped pupil (Fig. 3) and high-acuity and high-contrast imaging by the c-Si-PDA integrated with the FCPF (Fig. 4). Each feature was validated through imaging demonstrations with specific optical settings. The vertically uneven light condition was realized by placing a neutral density (ND) filter (GND16, K&F Concept, China) in front of a white light source. To make the polarized light noise, a commercial linear polarizer film (LPVISEX2, Thorlabs Inc., USA) was used. The c-Si-PDA was connected to a customized data acquisition system through the ACF. More details about the experimental setup for the imaging demonstration and the data acquisition system with built-in software are provided in Materials and Methods, fig. S19, and text S2.

A circular object with a vertical brightness gradient from top to bottom (Fig. 5B, top left inset) was used to demonstrate light-balancing capability. In the imaging result by the artificial vision system with the CPIS (Fig. 5Bi), the brightness of the captured object image decreased from top to bottom as the original object's brightness decreased. Conversely, the W-shaped pupil effectively diminished the most intense light at the top, balancing the overall light intensity in the vertical visual field (Fig. 5Bii). The profile graphs in the *y* fields (at 0° in the *x* fields) also show that the strong top lights were sufficiently dwindled in the WPIS in comparison with the CPIS (Fig. 5B, top right inset). Hence, the W-shaped pupil can enhance the image contrast under vertically uneven illumination conditions by balancing the brightness of the scene and reducing light saturation.

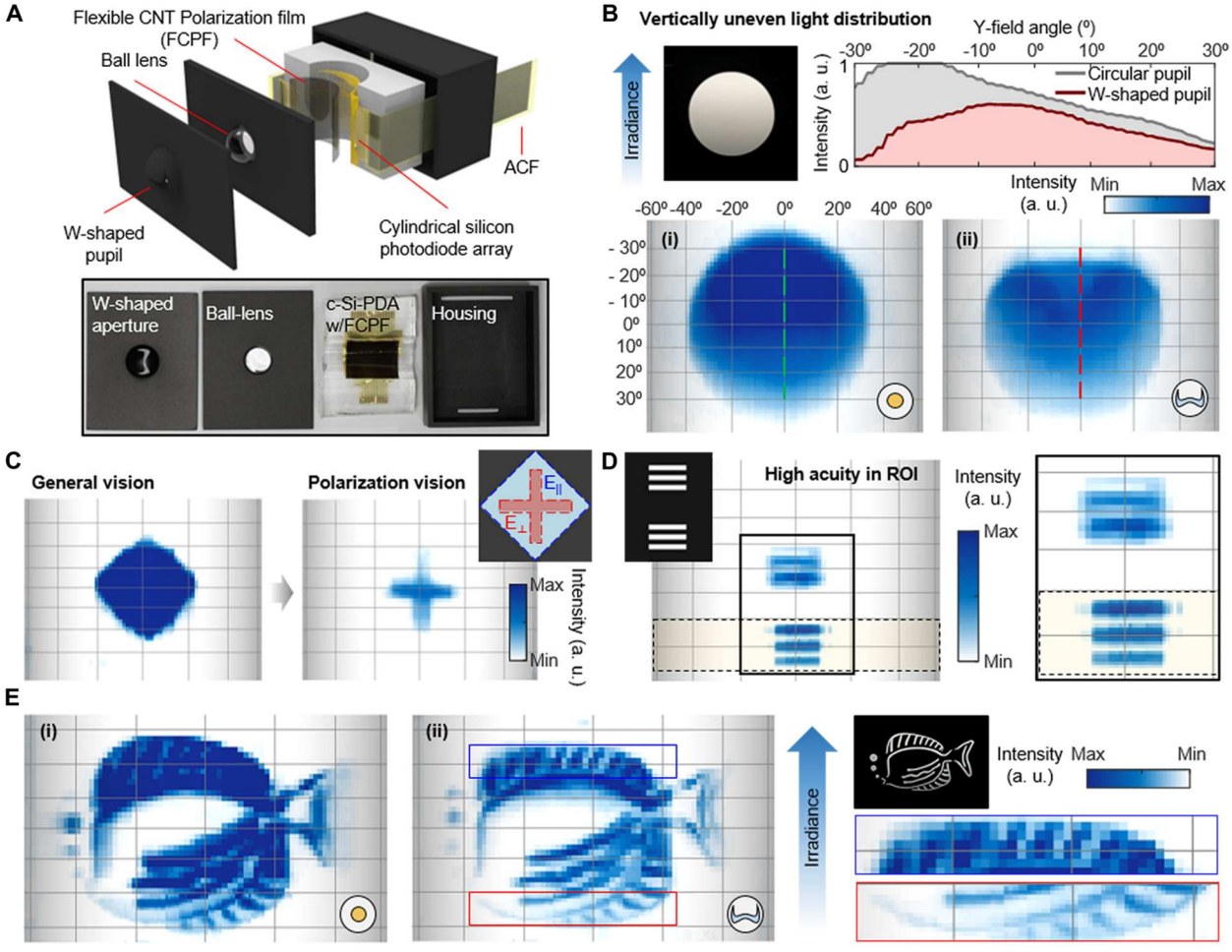

Fig. 5. Imaging demonstration by the cuttlefish eye–inspired artificial vision system. (**A**) Schematic illustration (top) and photographs (bottom) that show the components of the artificial vision system. (**B**) Imaging demonstration of the unevenly illuminated circular object by the artificial vision system with the circular (i, bottom left) and W-shaped (ii, bottom right) pupils. Inset: Original object image (top left) and intensity profiles for the circular pupil case (gray) and W-shaped pupil case (red) at the *y* field between −30° and 30° (at 0° in the *x* field) (top right). (**C**) Imaging demonstration of general vision (without FCPF) and polarization vision (with FCPF). Inset: Schematic illustration of the original object. The cross object and the peripheral diamond object illuminate polarized lights perpendicular to each other. (**D**) Left: A pair of linepair objects imaged by the low–pixel density region (top) and the high–pixel density region (bottom). Right: Magnified view of the boxed region. Left top inset: Original object image. (**E**) A fish-shaped object under vertically uneven illumination (top right inset) was imaged by the artificial vision system with a circular pupil (i) or with a W-shaped pupil (ii). Magnified views of the blue and red box region in Fig. 4Eii are presented on the right side.

In daytime, randomly polarized sunlight noise reflected from glazed surfaces of surroundings substantially reduces the imaging quality. In this case, polarization vision is useful to enhance detectability of the target object (*32*). We evaluated the polarization imaging capability of the artificial vision system using target objects prepared with polarized lights. First, a cross-shaped object was prepared, which radiated perpendicularly polarized light against the direction of aligned CNTs in the FCPF. Then, a diamond-shaped object surrounding the cross-shaped object was added, which radiated polarized light parallel to the direction of aligned CNTs. Whereas the cross-shaped object was veiled under the diamond-shaped object in general vision (i.e., c-Si-PDA without the FCPF) (Fig. 5C, left), the polarization vision (i.e., c-Si-PDA with the FCPF) could detect the cross-shaped object (Fig. 5C, right).

The pixel density is a key parameter that determines visual acuity (*33*), and the position of the high–pixel density region determines the main visual field (i.e., ROI). The artificial cuttlefish lens has a negative magnification, which forms an inverted image on the c-Si-PDA. Thus, the low visual field below the centerline of the horizon can be imaged with high acuity by the high–pixel density region above the centerline in the c-Si-PDA (fig. S14). We used line pair objects located on both the top and bottom sides of the centerline (Fig. 5D, left inset) to validate the high-acuity imaging in the ROI. A sharper image was captured for the bottom visual field by the high–pixel density region, whereas a blurry image was obtained for the top visual field by the low–pixel density region (Fig. 5D, magnified view in the right inset).

The uneven light-balancing and high-acuity imaging capability of the artificial vision system were successfully demonstrated in Fig. 5 (B and D). These capabilities could be shown more clearly

through an imaging demonstration of a more complex object. A fish-shaped image was captured by the artificial vision systems with either a circular pupil (Fig. 5Ei) or a W-shaped pupil (Fig. 5Eii). The original fish-shaped object (Fig. 5E, right inset) had a vertical gradient of light intensity, which dwindled from top to bottom. The W-shaped pupil effectively reduced the intensity of incident light from the top side, which enabled display of details of the fish′s fin (Fig. 5Eii). In contrast, the detailed fin shape was hard to recognize in the imaging result with the circular pupil (Fig. 5Ei). In addition, the right red box in Fig. 5E (magnified view of the red box in Fig. 5Eii, bottom) shows an image with a fine resolution captured by the high–density pixel region of the c-Si-PDA. However, the right blue box (magnified view of the blue box in Fig. 5Eii, top) shows a low-resolution image captured by the low-density pixel region of the c-Si-PDA.

DISCUSSION

Biological eyes have inherent optical strategies that have evolved with their natural habitats, and these could provide a technical breakthrough in artificial vision technologies in terms of compactness, high-performance imaging features (i.e., low optical aberrations and an ultrawide FOV), and unconventional form factors (i.e., full sphere form of the compound eye) (*4*, *17*, *34*, *35*). Cuttlefish eyes, unexplored natural eyes so far, inspired the development of an artificial vision system for mobile robotics and self-driving automobiles. In this study, we developed the cuttlefish eye–inspired artificial vision system, which is specially optimized to unfavorable optical environments, such as an uneven illumination and an excess of unnecessary information, by introducing the following features: a W-shaped pupil to balance vertically uneven illumination, polarization-sensitive vision to enhance the imaging contrast, and localized high pixel density for ROIs.

On the other hand, concerning industrial applications, further improvements remain in terms of a shape-adjustable pupil, polarization vision for every directional polarized light, and real-time object tracking. First, the pupils (i.e., W-shaped pupil and circular pupil as a control) of the current device were switched manually to analyze the light-balancing property. In nature, a cuttlefish modulates its pupil shape from circular to W according to the ambient light level (*20*). Because cuttlefish contract around 80% of the dilated pupil area in daytime (*21*), the artificial W-shaped pupil

Movie 1. Object detection of the cuttlefish eye–inspired artificial vision system. A dynamic object (i.e., a person on a motorcycle) under uneven illumination is detected on the simulated image sequence of the WPIS and CPIS. A red box appears when the target object is identified with a confidence of >0.8. The WPIS provides high-contrast imaging, which results in stable object detection.

has 20% of the opening area, enabling high-contrast imaging by balancing vertically uneven lights. A promising solution for 3D-adjustable pupils may be the use of light-actuated elastomers (*13*, *36*–*38*). Another approach may be to use a photochromic dye that changes light transmittance depending on external light intensity (*39*). The front lens surface with photochromic coating, except the W-shaped opening area, can be a light-sensitively shape-adjustable pupil.

The second relates to the undesirably missing data. Natural cephalopod vision systems (e.g., cuttlefish, squid, and octopus) recognize polarized lights by orthogonally stacked microvilli (*40*). Conversely, our current system only recognizes the polarized lights in a particular direction (i.e., parallel to the transmitted polarization direction of FCPF). Thus, the polarized lights perpendicular to the transmitted polarization direction of FCPF are blocked, which inevitably causes data loss. However, because most self-driving automobiles have exploited multiple cameras to prevent data loss (*41*), using multiple cuttlefish-inspired cameras with different polarization directions can solve the blind issue. In addition, the array of a photodiode unit with differently aligned polarizers (e.g., in-plane rotation angles of 0°, 45°, 90°, and 135°) can be another option to remove the invisibility of objects regardless of the polarization state (*42*–*44*).

Last, the fabrication technology gap between laboratories and industries hinders real-world applications such as object detection. The current version of the cuttlefish-inspired vision system demonstrated imaging performances in laboratory settings. The primary bottleneck for real-world imaging tests is the fabrication constraints in terms of photodiode size reduction at the university laboratory level. To compensate for such a limited pixel resolution, a customized mechanical system and iterative scanning process are required, which impede the real-time imaging demonstration. Nevertheless, current commercial image sensor fabrication technologies may enable the real-world applications of the proposed cuttlefish-inspired vision system. Additional imaging simulation results under ideal conditions of the WPIS (e.g., high resolution, color imaging, and high frame rate) also show that the WPIS could provide high-quality images for accurate object detection in an unfavorable optical environment, i.e., uneven illumination, compared with the CPIS (Movie 1 and Fig. 6) (see text S3 and table S4 for more details). The object-tracking strategy of vision systems depends on the properties of a target object and surrounding environments. Given that the moving object's trajectory is needed, high-quality and wide FOV vision systems are required. In this regard, the cuttlefish eye–inspired artificial vision system can provide object tracking within the horizontally wide FOV of 120°, which is suitable for surveillance in mobile robotics and artificial vision for self-driving. However, there is still room for further improvements in tracking objects out of sight by introducing mechanical movement systems such as biological eye movements.

MATERIALS AND METHODS

Artificial cuttlefish lens fabrication and specifications

Two half-ball lenses (N-BK7) and a precisely machined aperture stop (Unilate) were used to fabricate the artificial cuttlefish lens. A commercial half-ball lens with a diameter of 10 mm was selected (#45-937, Edmund Optics Inc.). The refractive index of N-BK7 is 1.52 at the wavelength of 588 nm. To assemble the components, an optical adhesive (NOA 61, Norland Products) filled in the space between the lenses and the aperture stop. The adhesive is transparent in the visible wavelength regime, and its refractive index is 1.56. The NOA 61 was brush-coated on the flat surface of the half-ball lens. The adhesive-coated half-ball lens was integrated on the aperture stop, and then the adhesive was cured under ultraviolet (UV) irradiation until fully solidified. The space on the opposite side of the aperture stop was filled with NOA 61, and another half-ball lens was fixed on the aperture stop by UV irradiation. The W-shaped pupil and circular pupil (Unilate) were precisely machined, and the pupil was assembled with the artificial cuttlefish lens.

Optical simulations for W-shaped pupil–integrated imaging system

The optical simulation was conducted using commercial ray tracing software (OpticStudio 16.0, Radiant ZEMAX LLC, USA). The minimum FOV of the artificial cuttlefish lens was selected as horizontally ±50° and vertically ±30°. The input wavelengths were selected in the visible spectrum range (486.1, 587.6, and 656.3 nm). The target focal length of the system was set to be higher than 1.5

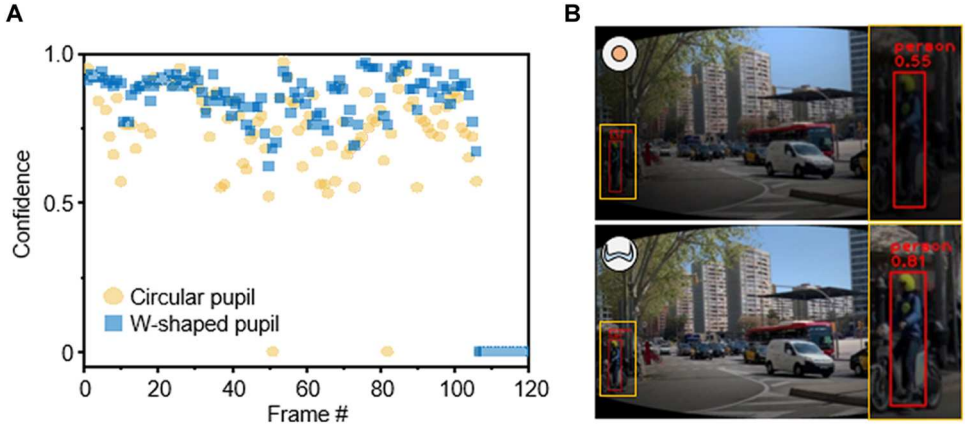

Fig. 6. The object detection results in imaging simulations for the W-shaped and circular pupils. (**A**) The scatter plot of confidence for W-shaped and circular pupils according to each simulated image. (**B**) Object detection results of simulated frames (frame no. 90) for the W-shaped and circular pupils. A person is detected with the confidence of 0.55 (top, circular pupil) and 0.81 (bottom, W-shaped pupil).

mm. The design optimization of the artificial cuttlefish lens was carried out. For the W-shaped pupil, a 2D layout was designed in a computer-aided design (CAD) program to extract coordinate data to convert the aperture shape, and then the W-shaped aperture was prepared. Meanwhile, a general circular aperture was used for the circular pupil. The toroidal surface with horizontal curvature was adopted as a cylindrical image plane. The optimization process was manually conducted by varying the focal length and horizontal curvature of the image plane. The designed artificial cuttlefish lens had a focal length of 1.606 mm, and the cylindrical image plane had a horizontal radius of curvature of −7.106 mm (table S2). The optical simulations were performed in the nonsequential mode for realizing uneven illumination objects (table S3). The number of rays for the analysis was 4×10^9, with a cosine exponent of 0.100 for the diffusive light source. Additional absorber surfaces were added between components to block scattered rays, which are blocked by a mechanical housing in practice. The 3D CAD part was designed as a cylindrical pixel array of 172 by 144 pixels and inserted in the software as a detector object. The single pixel size was set as (horizontal) 0.0921 mm by (vertical) 0.0938 mm. The software was initially designed to calculate and collect two intensity data in one pixel of the CAD object during the ray-tracing process. Therefore, we conducted additional postprocessing, averaging two simulated intensity data assigned on one pixel to match the intensity data collected by one pixel in practice.

Fabrication of the c-Si-PDA

The fabrication process (*45*, *46*) of the c-Si-PDA began with n-type and p-type doping of a silicon-on-insulator wafer (1.25-μm–thick top silicon; SOITEC) using thermal diffusion of spin-on dopants. The spin-coated n-type spin-on dopant (P509 solution, Filmtronics) was annealed at 200°C for 15 min, followed by thermal diffusion at 975°C for 12 min. The spin-coated p-type spin-on dopant (B153 solution, Filmtronics) was annealed at 200°C for 15 min, followed by thermal diffusion at 975°C for 30 min. The doped top silicon membrane of the silicon-on-insulator wafer was transfer-printed onto a polyimide (PI) layer (~1 μm in thickness; Sigma-Aldrich) spin-coated on the SiO_2 wafer. The desired active region of the silicon membrane was isolated using photolithography and dry etching. A series of fabrication processes, including spin coating of PI as an intermediate dielectric (~1 μm in thickness), patterning of the vertical interconnect access (via) using photolithography and dry etching, and depositing of Cr/Au metal electrodes (10/100 nm) using thermal evaporation and wet etching, were repeated twice. Another PI layer for the top encapsulation (~1 μm in thickness) was spin-coated and patterned using photolithography and dry etching. The fabricated c-Si-PDA was picked up using a water-soluble tape (3M Corp.) and transfer-printed onto the cylindrical polydimethylsiloxane (Dow Corning) mold. The fabricated polarization film was transfer-printed onto the surface of the c-Si-PDA for its integration with the c-Si-PDA.

Fabrication of the FCPF

The uniaxially aligned CNTs were embedded in a P(VDF-TrFE-CFE) film as a flexible optical polarizer. First, P3-SWCNTs (0.04 g; Carbon Solution Inc.) were dispersed in 2-butanone (10 ml; Sigma-Aldrich) by bath sonication for 2 hours. The solution was centrifuged at 8500 rpm for 15 min, and then the supernatant suspension was extracted. Then, the terpolymer of P(VDF-TrFE-CFE) (63.2/29.7/7.1 mole percent; Piezotech Arkema group) was dissolved in the suspension to be 8 weight % with mild heating at 60°C and magnetic stirring at 600 rpm. The CNT/ P(VDF-TrFE-CFE) solution was drop-cast onto a glass substrate and dried overnight to form a solid film in a vacuum chamber at room temperature. The dried film was peeled off from the glass substrate. The film thickness was 50 μm. It was laminated to another film at 110°C to stack multiple layers using a thermal laminator (PhotoLami-3500 plus, Hyundai Office LLC). The stacked film (4.7 cm by 3.5 cm) was then mechanically stretched by applying mild heat until the film was four times longer than the initial length. The film was heated for 3 min to release the stress and left for >12 hours while the stretching tension was maintained until the film was fixed. Then, the FCPF was cut into a rectangular shape (dimensions, 1.8 mm by 2.5 mm) to fully cover the active area of the c-Si-PDA.

Imaging demonstration of cuttlefish eye–inspired artificial vision

The imaging demonstration setup was prepared to verify light-balancing and polarization vision features. A commercial ND filter (GND GND16, K&F Concept, China) was integrated on a white diffusive light-emitting diode panel to set up the vertically uneven illumination. To make the polarization noise, we placed a commercial linear polarizer film (LPVISEX2, Thorlabs Inc., USA) in front of the light source in a perpendicular direction to the polarization axis of the FCPF on the c-Si-PDA. A scanning method was used to improve the entire imaging resolution via linear and rotational movements of the c-Si-PDA. The movement was from −0.4 to 0.4 mm in the linear y direction and from −4.6° to 4.6° in the rotational direction with the increment of 0.08 mm and 0.92°, respectively. A motorized linear actuator (CMA-12CCCL, Newport, USA) and rotator (PR-50C, Newport, USA) were used for precise movement, which was controlled by the motorization stage controller (ESP7000, Newport, USA). The data acquisition board collected the imaging data in real time and processed them with MATLAB (MathWorks Inc., USA) (see text S2 for more details).

Supplementary Materials

This PDF file includes:

Texts S1 to S3
Figs. S2 to S19
Tables S1 to S4
References (*47*–*56*)

REFERENCES AND NOTES

1. M. Hirz, B. Walzel, Sensor and object recognition technologies for self-driving cars. *Comput. Des. Appl.* **15**, 501–508 (2018).
2. L. Liu, S. Lu, R. Zhong, B. Wu, Y. Yao, Q. Zhang, W. Shi, Computing systems for autonomous driving: State-of-the-art and challenges. *IEEE Internet Things J.* **8**, 6469–6486 (2020).
3. Z. Chen, Z. Zhang, F. Dai, Y. Bu, H. Wang, Monocular vision-based underwater object detection. *Sensors* **17**, 1784 (2017).
4. M. Kim, G. J. Lee, C. Choi, M. S. Kim, M. Lee, S. Liu, K. W. Cho, H. M. Kim, H. Cho, M. K. Choi, N. Lu, Y. M. Song, D.-H. Kim, An aquatic-vision-inspired camera based on a monocentric lens and a silicon nanorod photodiode array. *Nat. Electron.* **3**, 546–553 (2020).
5. J. Wei, J. M. Snider, J. Kim, J. M. Dolan, R. Rajkumar, B. Litkouhi, Towards a viable autonomous driving research platform, in *2013 IEEE Intelligent Vehicles Symposium (IV)*, Gold Coast, QLD, Australia, 23 to 26 June 2013 (IEEE, 2013), pp. 763–770.
6. N. Paul, C. Chung, Application of HDR algorithms to solve direct sunlight problems when autonomous vehicles using machine vision systems are driving into sun. *Comput. Ind.* **98**, 192–196 (2018).

7. K. Yoneda, N. Suganuma, R. Yanase, M. Aldibaja, Automated driving recognition technologies for adverse weather conditions. *IATSS Res.* **43**, 253–262 (2019).
8. O. K. Soni, J. S. Kumare, A survey on underwater images enhancement techniques, in *2020 IEEE 9th International Conference on Communication Systems and Network Technologies (CSNT)*, Gwalior, India, 10 to 12 April 2020 (IEEE, 2020), pp. 333–338.
9. A. Takács, I. Rudas, D. Bösl, T. Haidegger, Highly automated vehicles and self-driving cars [industry tutorial]. *IEEE Robotics Autom. Mag.* **25**, 106–112 (2018).
10. D. J. Yeong, G. Velasco-Hernandez, J. Barry, J. Walsh, Sensor and sensor fusion technology in autonomous vehicles: A review. *Sensors* **21**, 2140 (2021).
11. F. Liao, Z. Zhou, B. J. Kim, J. Chen, J. Wang, T. Wan, Y. Zhou, A. T. Hoang, C. Wang, J. Kang, J.-H. Ahn, Y. Chai, Bioinspired in-sensor visual adaptation for accurate perception. *Nat. Electron.* **5**, 84–91 (2022).
12. L. Gu, S. Poddar, Y. Lin, Z. Long, D. Zhang, Q. Zhang, L. Shu, X. Qiu, M. Kam, A. Javey, Z. Fan, A biomimetic eye with a hemispherical perovskite nanowire array retina. *Nature* **581**, 278–282 (2020).
13. S. Petsch, S. Schuhladen, L. Dreesen, H. Zappe, The engineered eyeball, a tunable imaging system using soft-matter micro-optics. *Light. Sci. Appl.* **5**, –e16068 (2016).
14. Z. Rao, Y. Lu, Z. Li, K. Sim, Z. Ma, J. Xiao, C. Yu, Curvy, shape-adaptive imagers based on printed optoelectronic pixels with a kirigami design. *Nat. Electron.* **4**, 513–521 (2021).
15. H. Liu, Y. Huang, H. Jiang, Artificial eye for scotopic vision with bioinspired all-optical photosensitivity enhancer. *Proc. Natl. Acad. Sci.* **113**, 3982–3985 (2016).
16. A. Altaqui, P. Sen, H. Schrickx, J. Rech, J.-W. Lee, M. Escuti, W. You, B. J. Kim, R. Kolbas, B. T. O'Connor, M. Kudenov, Mantis shrimp–inspired organic photodetector for simultaneous hyperspectral and polarimetric imaging. *Sci. Adv.* **7**, eabe3196 (2021).
17. M. Lee, G. J. Lee, H. J. Jang, E. Joh, H. Cho, M. S. Kim, H. M. Kim, K. M. Kang, J. H. Lee, M. Kim, H. Jang, J.-E. Yeo, F. Durand, N. Lu, D.-H. Kim, Y. M. Song, An amphibious artificial vision system with a panoramic visual field. *Nat. Electron.* **5**, 452–459 (2022).
18. Y. Wu, Y. Liu, Y. Zhou, Q. Man, C. Hu, W. Asghar, F. Li, Z. Yu, J. Shang, G. Liu, M. Liao, R.-W. Li, A skin-inspired tactile sensor for smart prosthetics. *Sci. Robot.* **3**, eaat0429 (2018).
19. M. Han, X. Guo, X. Chen, C. Liang, H. Zhao, Q. Zhang, W. Bai, F. Zhang, H. Wei, C. Wu, Q. Cui, S. Yao, B. Sun, Y. Yang, Q. Yang, Y. Ma, Z. Xue, J. W. Kwak, T. Jin, Q. Tu, E. Song, Z. Tian, Y. Mei, D. Fang, H. Zhang, Y. Huang, Y. Zhang, J. A. Rogers, Submillimeter-scale multimaterial terrestrial robots. *Sci. Robot.* **7**, eabn0602 (2022).
20. L. M. Mäthger, R. T. Hanlon, J. Håkansson, D.-E. Nilsson, The W-shaped pupil in cuttlefish (*Sepia officinalis*): Functions for improving horizontal vision. *Vision Res.* **83**, 19–24 (2013).
21. F. Schaeffel, C. J. Murphy, H. C. Howland, Accommodation in the cuttlefish (Sepia officinalis). *J. Exp. Biol.* **202**, 3127–3134 (1999).
22. Z.-L. Hao, X.-M. Zhang, H. Kudo, M. Kaeriyama, Development of the retina in the cuttlefish *Sepia esculenta*. *J. Shellfish. Res.* **29**, 463–470 (2010).
23. N. Watanuki, G. Kawamura, S. Kaneuchi, T. Iwashita, Role of vision in behavior, visual field, and visual acuity of cuttlefish *Sepia esculenta*. *Fish. science* **66**, 417–423 (2001).
24. C. M. Talbot, J. N. Marshall, The retinal topography of three species of coleoid cephalopod: Significance for perception of polarized light. *Philos. Transactions R. Soc. B: Biol. Sci.* **366**, 724–733 (2011).
25. N. Shashar, P. Rutledge, T. Cronin, Polarization vision in cuttlefish in a concealed communication channel? *J. Exp. Biol.* **199**, 2077–2084 (1996).
26. L. M. Mathger, N. Shashar, R. T. Hanlon, Do cephalopods communicate using polarized light reflections from their skin? *J. Exp. Biol.* **212**, 2133–2140 (2009).
27. W. S. Jagger, P. J. Sands, A wide-angle gradient index optical model of the crystalline lens and eye of the octopus. *Vision Res.* **39**, 2841–2852 (1999).
28. R. H. Douglas, R. Williamson, H.-J. Wagner, The pupillary response of cephalopods. *J. Exp. Biol.* **208**, 261–265 (2005).
29. S. Q. Duntley, Light in the sea. *J. Opt. Soc. Am.* **53**, 214–233 (1963).
30. S. Shoji, H. Suzuki, R. P. Zaccaria, Z. Sekkat, S. Kawata, Optical polarizer made of uniaxially aligned short single-wall carbon nanotubes embedded in a polymer film. *Phys. Rev. B* **77**, 153407 (2008).
31. H. Ajiki, T. Ando, Aharonov-Bohm effect in carbon nanotubes. *Phys. B. Condens. Matter* **201**, 349–352 (1994).
32. W. Fan, S. Ainouz, F. Meriaudeau, A. Bensrhair, Polarization-based car detection, in *2018 25th IEEE International Conference on Image Processing (ICIP)*, Athens, Greece, 7 to 10 October 2018 (IEEE, 2018), pp. 3069–3073.
33. J. Van der Spiegel, G. Kreider, C. Claeys, I. Debusschere, G. Sandini, P. Dario, F. Fantini, P. Bellutti, G. Soncini, A foveated retina-like sensor using CCD technology, in *Analog VLSI Implementation of Neural Systems* (Springer, 1989), pp. 189–211.
34. H. C. Ko, M. P. Stoykovich, J. Song, V. Malyarchuk, W. M. Choi, C.-J. Yu, J. B. Geddes III, J. Kiao, S. Wang, Y. Huang, J. A. Rogers, A hemispherical electronic eye camera based on compressible silicon optoelectronics. *Nature* **454**, 748–753 (2008).
35. Y. M. Song, Y. Xie, V. Malyarchuk, J. Xiao, I. Jung, K.-J. Choi, Z. Liu, H. Park, C. Lu, R.-H. Kim, R. Li, K. B. Crozier, Y. Huang, J. A. Rogers, Digital cameras with designs inspired by the arthropod eye. *Nature* **497**, 95–99 (2013).
36. H. Zeng, O. M. Wani, P. Wasylczyk, F. Kaczmarek, A. Riimagi, Self-regulating iris based on light-actuated liquid crystal elastomer. *Adv. Mater.* **29**, 1701814 (2017).
37. K. T. Chang, C. Y. Liu, J. H. Liu, Tunable artificial iris controlled by photo/thermal exposure based on liquid crystalline elastomers. *Macromol. Mater. Eng.* **306**, 2100121 (2021).
38. S. Martin, A. Bruns, J. Franke, Dynamic light control using bionic dielectric elastomer iris actuators. *Adv. Funct. Mater.* **32**, 2112260 (2022).
39. H. Torres-Pierna, D. Ruiz-Molina, C. Roscini, Highly transparent photochromic films with a tunable and fast solution-like response. *Mater. Horiz.* **7**, 2749–2759 (2020).
40. N. Shashar, C. A. Milbury, R. T. Hanlon, Polarization vision in cephalopods: Neuroanatomical and behavioral features that illustrate aspects of form and function. *Mar. Freshw. Behav. Physiol.* **35**, 57–68 (2002).
41. C. Häne, L. Heng, G. H. Lee, F. Fraundorfer, P. Furgale, T. Sattler, M. Pollefeys, 3D visual perception for self-driving cars using a multi-camera system: Calibration, mapping, localization, and obstacle detection. *Image Vis. Comput.* **68**, 14–27 (2017).
42. M. Garcia, C. Edmiston, R. Marinov, A. Vail, V. Gruev, Bio-inspired color-polarization imager for real-time in situ imaging. *Optica* **4**, 1263–1271 (2017).
43. V. Gruev, R. Perkins, T. York, CCD polarization imaging sensor with aluminum nanowire optical filters. *Opt. Express* **18**, 19087–19094 (2010).
44. A. Basiri, X. Chen, J. Bai, P. Amrollahi, J. Carpenter, Z. Holman, C. Wang, Y. Yao, Nature-inspired chiral metasurfaces for circular polarization detection and full-stokes polarimetric measurements. *Light Sci. Appl.* **8**, 78 (2019).
45. A. K. Katiyar, A. A. Davidson, H. Jang, Y. Hwangbo, B. Han, S. Lee, Y. Hagiwara, T. Shimada, H. Hirakata, T. Kitamura, J.-H. Ahn, Ultrasoft silicon nanomembranes: Thickness-dependent effective elastic modulus. *Nanoscale* **11**, 15184–15194 (2019).
46. J. Li, R. Li, C.-H. Chiang, Y. Zhong, H. Shen, E. Song, M. Hill, S. M. Won, K. J. Yu, J. M. Baek, Y. Lee, J. Viventi, Y. Huang, J. A. Rogers, Ultrathin, high capacitance capping layers for silicon electronics with conductive interconnects in flexible, long-lived bioimplants. *Adv. Mater. Technol.* **5**, 1900800 (2020).
47. P. Jereb, C. F. E. Roper, *Cephalopods of the World. An Annotated and Illustrated Catalogue of Species Known to Date. Volume 1. Chambered Nautiluses and Sepioids (Nautilidae, Sepiidae, Sepiolidae, Sepiadariidae, Idiosepiidae, and Spirulidae)* (FAO, 2005).
48. P. Jereb, C. F. E. Roper, M. D. Norman, J. K. Finn, *Cephalopods of the World. An Annotated and Illustrated Catalogue of Species Known to Date. Volume 3. Octopods and Vampire Squids* (FAO, 2016).
49. P. Jereb, C. F. E. Roper, *Cephalopods of the World. An Annotated and Illustrated Catalogue of Species Known to Date. Volume 2. Myopsid and Oegopsid Squids* (FAO, 2010).
50. C. M. Talbot, J. Marshall, Polarization sensitivity and retinal topography of the striped pyjama squid (*Sepioloidea lineolata*–Quoy/Gaimard 1832). *J. Exp. Biol.* **213**, 3371–3377 (2010).
51. F. D. Hanke, A. Kelber, The eye of the common octopus (*Octopus Vulgaris*). *Front. Physiol.* **10**, 1637 (2020).
52. L. R. McCormick, J. H. Cohen, Pupil light reflex in the Atlantic brief squid, *Lolliguncula brevis*. *J. Exp. Biol.* **215**, 2677–2683 (2012).
53. M. S. Banks, W. W. Sprague, J. Schmoll, J. A. Q. Parnell, G. D. Love, Why do animal eyes have pupils of different shapes? *Sci. Adv.* **1**, e150039 (2015).
54. A. Makino, T. Miyazaki, Topographical distribution of visual cell nuclei in the retina in relation to the habitat of five species of Decapodiformes (Cephalopoda). *J. Moll. Stud.* **76**, 180–185 (2010).
55. A. Bochkovskiy, C. Wang, H. Liao, Yolov4: Optimal speed and accuracy of object detection. arXiv, 2004.10934 (2020).
56. T.-Y. Lin, M. Maire, S. Belongie, J. Hays, P. Perona, D. Ramanan, P. Dollár, C. L. Zitnick, Microsoft COCO: Common objects in context. in *Computer Vission–ECCV 2014*, D. Fleet, T. Pajdla, B. Shiele, T. Tuytelaars, Eds. (Springer, 2014), vol. 8693, pp. 740–755.

Acknowledgments: We are grateful to the reviewers for valuable and critical feedback on this manuscript. **Funding:** This work was supported by the National Research Foundation (NRF) of Korea (2017M3D1A1039288/2018R1A4A1025623). This work was also supported by the Institute for Basic Science (IBS-R006-A1). **Author contributions:** Minsung Kim, S.C., Minsu Kim, G.J.L., D.-H.K., and Y.M.S. designed the experiments, analyzed the data, and wrote the paper. Minsung Kim and Minsu Kim fabricated the photodiode array and performed characterization of individual devices. S.C., G.J.L., M.S.K., and J.-E.Y. fabricated the lens optics and the polarization film and performed theoretical analysis on optics. All authors discussed the results and commented on the manuscript. **Competing interests:** The authors declare that they have no competing interests. **Data and materials availability:** All data needed to support the conclusions of this manuscript are included in the main text or Supplementary Materials.

Submitted 18 August 2022
Accepted 18 January 2023

Published 15 February 2023
10.1126/scirobotics.ade4698

Science Robotics

Cuttlefish eye–inspired artificial vision for high-quality imaging under uneven illumination conditions

Minsung Kim, Sehui Chang, Minsu Kim, Ji-Eun Yeo, Min Seok Kim, Gil Ju Lee, Dae-Hyeong Kim, and Young Min Song

Sci. Robot., **8** (75), eade4698.
DOI: 10.1126/scirobotics.ade4698